Supporting Information

Versatile Ionic Liquid Gels Formed by Dynamic Covalent Bonding and Microphase Separated Structures

Zeyu Zhang, [a] Xin Zhao, [a] Xing Song, [b] Dejun Peng, [a] Shixue Ren,*[a] Junxue Ren,*[b] Yanli Ma [a] and Shujun Li [a]

[a.] Key Laboratory of Bio-based Material Science & Technology（Northeast Forestry University）Ministry of Education, School of Materials Science and Engineering, Northeast Forestry University, Harbin 150040, China.

[b] School of Astronautics, Beihang University, Beijing, 102206，China.

1 Preparation and characterization of Ionic liquid gel

1.1 Materials

Polycaprolactone diol (PCL2000, Mw~2000), polycaprolactone diol (PCL530, Mw~530) were purchased from Aladdin (China)., dried in vacuum at 115 °C for 1.5 h before use, and cooled to 40-60 °C for spare. Isophorone diisocyanate (IPDI, 99%), dimethylethylene glyoxime (DMG, AR, 98%), 2,6-pyridinedimethanol (PDM, 97%), rutin (R, 95%), 1-ethyl-3-methylimidazolium bis(trifluoromethanesulfonyl)imide salt ([EMIM][NTf$_2$], 97%), and dibutyltin dilaurate (DBTDL, 95%) were purchased from Aladdin (China)., and other solvents were purchased from Sinopharm Chemical Reagent Company (China). All reagents were used as received without further purification. X80 pipeline steels (10 mm × 10 mm × 3 mm) abraded by 120#, 400#, 1000# SiC sandpapers and cleaned by absolute ethanol and acetone were acted as substrates. were acted as substrates. Artificial seawater, purchased from Zhongyuan Technology 188 Co (China). Quartz sand (0.5-1mm), purchased from Yixinglong Environmental Protection Technology Co(China). Soil was obtained from Harbin City, Heilongjiang Province, China.

1.2 Synthesis of ionic liquid gels

The required equivalents of PCL2000, PCL530, DMG (0.0929 g, 0.8 mmol) and [EMIM][NTf$_2$] (40 wt.%) were dissolved in acetone (8 mL) and the mixture was stirred at 50 °C until everything was completely dissolved. IPDI (1.585 mL, 7.6 mmol) and DBTDL (0.5 wt.%) were added and the mixture was stirred at 50 °C under nitrogen for 30 min to provide linear NCO-terminated polyurethane prepolymer. PDM (0.1113 g, 0.8 mmol) was then added and stirring was continued at 50 °C for 30 min. Rutin (0.2442 g, 0.4 mmol) and acetone (8 mL) were added and the mixture was allowed to react at 50 °C for 1 h under nitrogen. The reaction mixture was then poured into a PTFE mold, allowed to stand at 50 °C for 24 h, and then further cured in a vacuum oven at 70 °C for 24 h to give the ionic liquid gel. Ionic liquid gels with P and R ratios of 40:1, 68:1, 96:1 and 124:1 were prepared using this method.

1.3 Characterization

1.3.1 General characterization

^{1}H-NMR spectra were recorded using a 400 MHz Bruker AVANCE III spectrometer (Bruker Instruments), with DMSO-d$_6$ as the solvent. FT-IR spectra were recorded at room temperature using a Nicolet iN10 FT-IR spectrometer (America Instruments). The resolution was 32 scans and the

scan range was 4000–400 cm^{-1}. Differential scanning calorimetry (DSC) of the samples was carried using a Netzsch DSC 200 F3 differential scanning calorimeter (Bruker Instruments). All samples were heated from −120 to 80 °C with a scan rate of 10 °C min^{-1}. The glass transition temperatures and loss factor curves of the samples were investigated using a Q800 dynamic mechanical analyzer (TA Instruments, New Castle, DE, USA). Measurements were recorded over the temperature range −100 to 100 °C, with a ramp rate of 3 °C min^{-1} and a frequency of 1 Hz. The sample using a Discovery TGA 550 thermo-gravimetric analyzer (TA Instruments). An alumina crucible was used and the sample was heated from 30 to 800 °C at a rate of 20 °C min^{-1} under a nitrogen atmosphere. Transparency tests were carried out using a TU-1950 UV-Vis spectrophotometer, with a scanning range from 800 to 200 nm, using air as the reference. X-ray diffraction (XRD) maps were recorded using a Panalytical X'Pert Pro X-ray diffractometer (Holland Instruments). Data were acquired over the range 10–80°, with a scanning speed of 10° min^{-1}. An Apreo S HiVac scanning electron microscope (SEM) was used to examine the surface structure of the samples. A Bruker Dimension Icon atomic force microscope was used to examine the phase diagrams of the samples (1 × 1 um^2). Temperature scanning of the ionic liquid gels (thickness 1 mm) was carried out using a Haake Mars 60 rheometer (ThermoFisher). A 15 mm diameter parallel plate test system was used for temperature scanning, at a constant strain of 0.1%, a constant frequency of 10 rad s^{-1} and a test temperature range of 25–200 °C, with a temperature increase/decrease rate of 5 °C min^{-1}. A parallel plate with a diameter of 15 mm was also used for frequency testing at a constant strain of 0.1%, a test temperature of 25 °C and 50 °C, and a frequency variation range of 0.01–100 Hz.

1.3.2 Tensile tests

Stress-strain curves were measured using a UTM2203 electronic universal testing machine. The samples were cut into dumbbell shapes (20 mm × 4.0 mm × 1 mm) for testing. The tensile rate was set at 50 mm min^{-1}. Cyclic tensile profiles were measured using INSTRON 5982 (America Instruments) electronic universal testing machines. The samples were cut into dumbbell shapes (20 mm × 4.0 mm × 1 mm) for testing and cyclic tensile deformation was determined by gradually increasing the tensile strain, with the strain rate fixed at 10 mm min^{-1}. In each step, once the sample reached 200% tensile strain, the coupler orientation was reversed and the sample strain was released at the same rate as it had been applied until zero strain was reached. The coupler was then immediately reversed and the stretch repeated. Alternatively, the sample was stretched to 200%

strain, left for 1, 10, 30, 60, or 120 min at room temperature and then stretched for a new cycle. In addition to these different strain cycles, the sample was stretched to 200% strain for 5 cycles or 50% strain for 500 cycles with a waiting time of 0 min between each cycle.

Stress relaxation curves were measured using a UTM2203 electronic universal testing machine. The samples were cut into dumbbell shapes (20 mm × 4.0 mm × 1 mm) for testing and kept at room temperature, with a fixed strain of 10% and a relaxation time of 10 min. The dissipated energy, which is the area of the hysteresis curve of the ionic liquid gel during loading and unloading and during stress relaxation, was calculated using Origin software.

1.3.3 Determination of adhesion toughness value (adhesion stripping test)

The ionic liquid gel was bonded to a high-strength steel plate and an adhesive peel test was then carried out using a UTM2203 universal electronic testing machine. The adhesive bonding toughness of the gel was measured in accordance with the ASTMD 2861 standard (90° adhesive peeling test). The specific process was as follows: the size of the metal plate was 76.2 mm × 127 mm × 3.2 mm, the size of the double network hydrogel specimen was 110 mm × 30 mm × 2 mm, and the double network hydrogel specimen was bonded to the metal plate. The metal plates were fixed, and one end of the gel specimen was clamped using a material mechanical testing machine and a 90° adhesive peeling test was carried out at a rate of 50 mm min^{-1}. Once the mechanical testing machine reading F was stabilized, its value was divided by the width of the hydrogel specimen to obtain the adhesive bonding toughness value of the gel.

1.3.4 Adhesion tests

The sample was hot-melted and applied between the two substrates. The substrates were tightened with clamps and left at room temperature for 24 h. Adhesion strength-displacement curves were measured using a UTM2203 electronic universal testing machine. The tensile rate was set at 50 mm min^{-1} and adhesion strength was calculated by dividing the maximum force by the adhesion area. To test the adhesion of gels to high-strength steel in aqueous media, a bonded sample was left underwater for 30 s and then used to pull a 2 kg weight out of the water.

1.3.5 Simulation of bonding process

A two-dimensional finite element model was used to simplify simulation of the 90° peeling experimental setup for bonding gels onto solid substrates to obtain the corresponding geometric model. After several attempts, a structure that was easy to converge was chosen (Fig. 3g) to prevent

the model unit from failing because of excessive bending. The geometry of the gel layer met the actual experimental requirements [1], i.e., a thickness of 3 mm and a length of 80 mm, with the corresponding substrate having a thickness of 1 mm and a length of 80 mm. A portion of the hydrogel layer was not initially bonded to the substrate and was used for clamping during the peeling test.

The deformation of the system was assumed to be in a plane strain state, i.e., the strain in the direction perpendicular to this surface was neglected. Numerical simulations were carried out using ANSYS/Static Structural Simulation software, where the ionic liquid gel, rigid substrate and liner were simulated using the Plane183 unit and the cohesive interface was simulated using the CONTA175 unit.

1.3.6 Electrochemical corrosion tests

Electrochemical tests to evaluate the corrosion resistance of the samples were carried out using a VersaStat 4 electrochemical workstation. A standard three-electrode system in 3.5wt.% NaCl solution was used, with a platinum electrode as the counter electrode and a saturated calomel electrode as the reference electrode. The polarization (Tafel) curves of the samples were measured over the scanning range −1.2 to 0.2 V. The electrochemical parameters, corrosion potential (E_{corr}), corrosion current density (I_{corr}) and corrosion inhibition efficiency (η) were fitted by Tafel linear extrapolation (Table S4), and the corrosion inhibition efficiency (η) was calculated as

$$\eta(\%) = \frac{I_{corr}^{0} - I_{corr}}{I_{corr}^{0}} \times 100 \ (1)$$

Electrochemical impedance spectra of the samples were collected over the range 10^5 to 10^{-2} Hz. Electrochemical tests were performed after the samples had been immersed in 3.5 wt.% NaCl solution for 7 days. The dynamic processes in marine and soil environments were also simulated to confirm the long-term corrosion protection. Fine sand ($\Phi = 0.5$–1 mm, 12 g L^{-1} mass fraction) was added to seawater and stirred at 80 r min^{-1} to simulate a marine environment. The coated and uncoated steel plates were also buried in soil in a crystallization dish and left for 14 days before observing surface changes.

2. Supplementary Figures
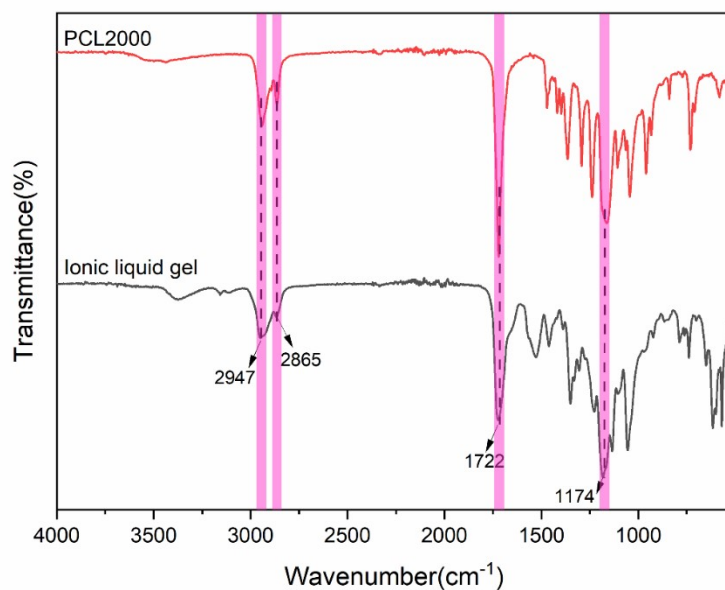
Fig. S1 FT-IR spectra of DI-PR and PCL2000. The absorption peak corresponding to the symmetric stretching vibration of C-O-C in PCL appears at 1174 cm^{-1}, the same absorption peak due to -C=O in PCL is at 1722 cm^{-1}, the peak due to asymmetric stretching of -CH$_2$ in PCL is at 2947 cm^{-1}, and the symmetric stretching vibrational peak due to -CH$_2$ in PCL is at 2865 cm^{-1}.
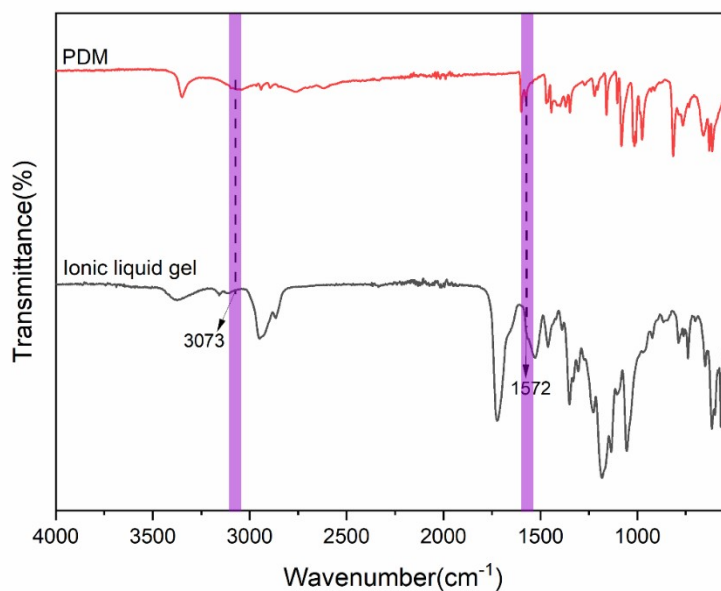

Fig. S2 FT-IR spectra of DI-PR and PDM. The absorption peak due to stretching vibration of the aryl ring is at 1572 cm^{-1} (skeleton band) and the peak due to C-H stretching vibration of the PDM aziridine ring appears at 3073 cm^{-1}.
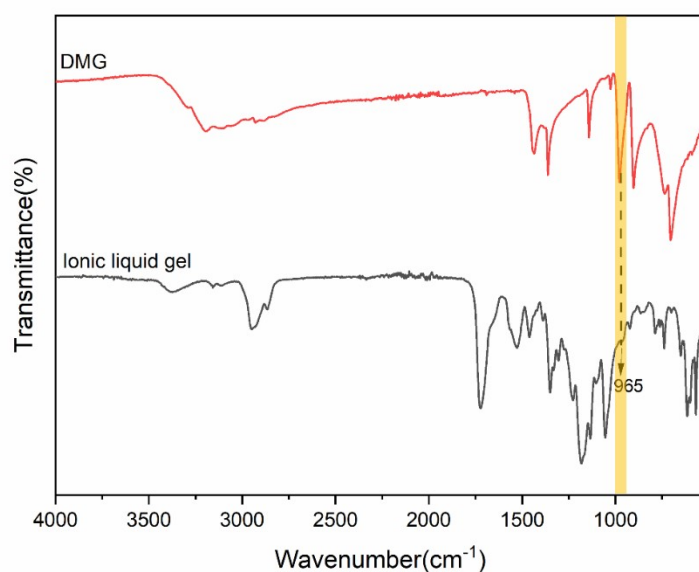
Fig. S3 FT-IR spectra of DI-PR and DMG. The absorption peak due to stretching vibration of N-O in the dimethylglyoxime unit is at 960 cm^{-1}.
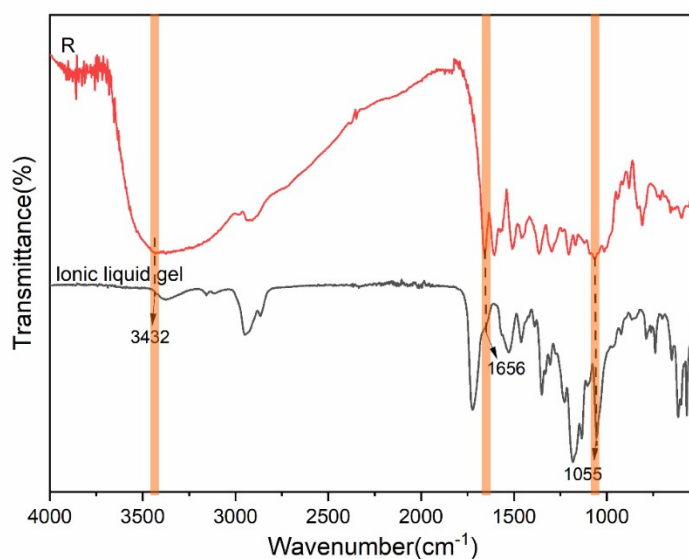
Fig. S4 FT-IR spectra of DI-PR and rutin. The peaks at 1656 and 1055 cm^{-1} in the spectrum of DI-PR, due to stretching vibrations of the C=O bond and C-O-C of the six-atom cyclic ether in rutin, respectively, proved the successful cross-linking of rutin. The absence of the vibrational absorption peaks due to the -OH groups of rutin at 3432 cm^{-1} in the spectrum of DI-PR demonstrated that the cross-linking was essentially complete.
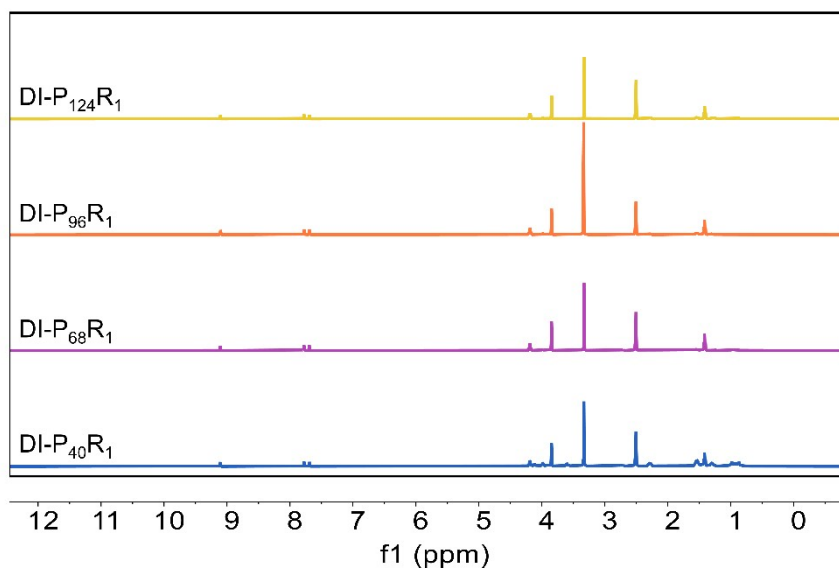
Fig. S5 ^{1}H-NMR spectra of different DI-PR ionic gels. Chemical shifts of hydrogen at δ = 7.8, 7.7, and 9.1 ppm correspond to amide groups formed by IPDI linking to PCL, DMG and PDM, respectively.
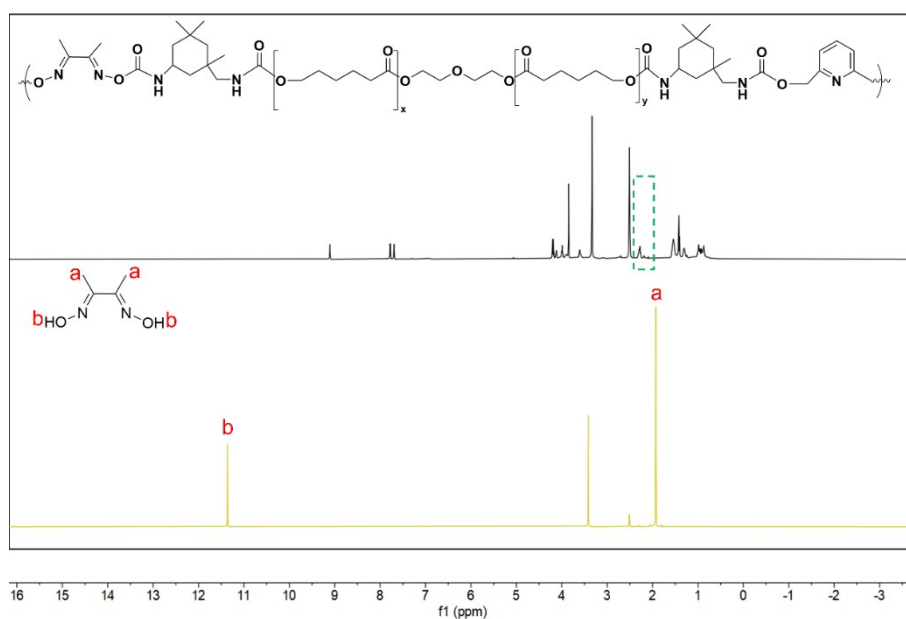
Fig. S6 ^{1}H-NMR spectra of DI-PR and DMG. The chemical shift of the methyl group attached to the oxime group is at δ = 2.2 ppm, and the chemical shift of the hydroxyl hydrogen in DMG is at δ = 11.3 ppm.
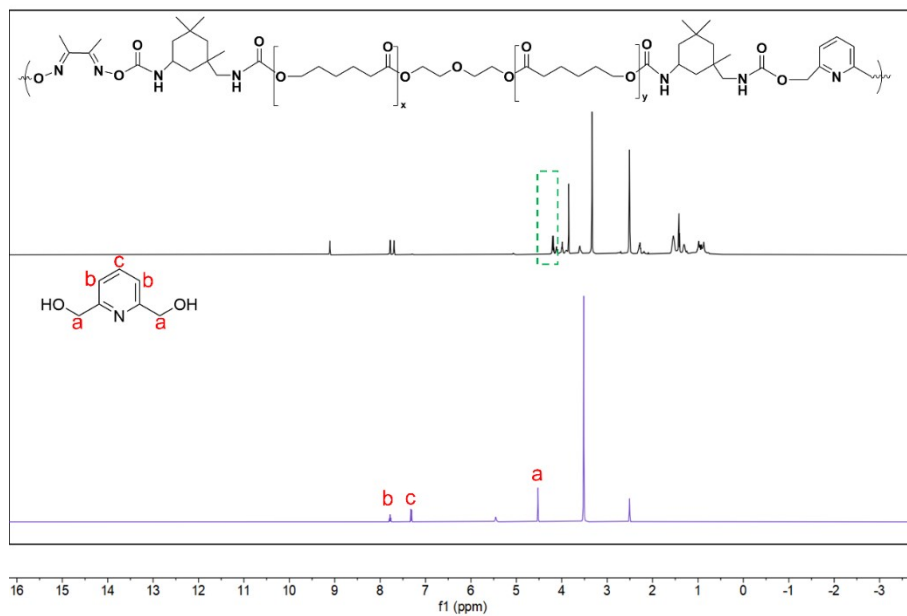
Fig. S7 ^{1}H-NMR spectra of DI-PR and PDM. The chemical shift of the methylene group of PDM linked to IPDI appears at δ = 3.9 ppm; peaks a, b, c correspond to the labeled hydrogens of PDM, and the absence of those peaks in the spectrum of the gel demonstrates successful access of the chain extender.
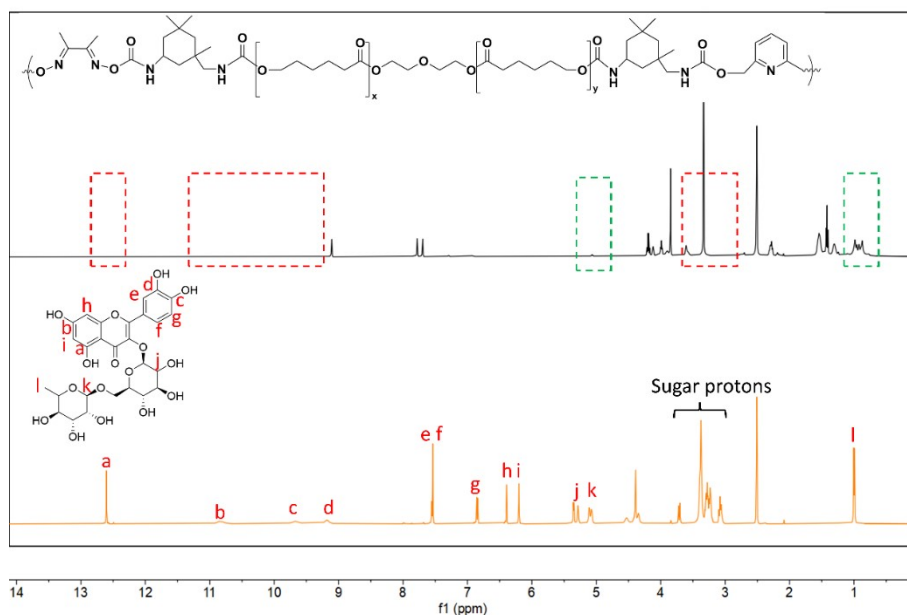
Fig. S8 ^{1}H-NMR spectra of DI-PR and rutin. Peaks due to protons of the aromatic hydroxyl groups of rutin are at δ = 12.6 (a), 10.8 (b), 9.7 (c), and 9.2 (d). Peaks due to the sugar protons of rutin are at δ = 3.0–3.8 ppm. Peaks labeled e, f, g, h, i, j, k, and l are due to the corresponding protons as labeled in the structure of rutin. The absence of these peaks in the spectrum of DI-PR demonstrate that the hydroxyl group of rutin reacts with IPDI to form a cross-linked structure.
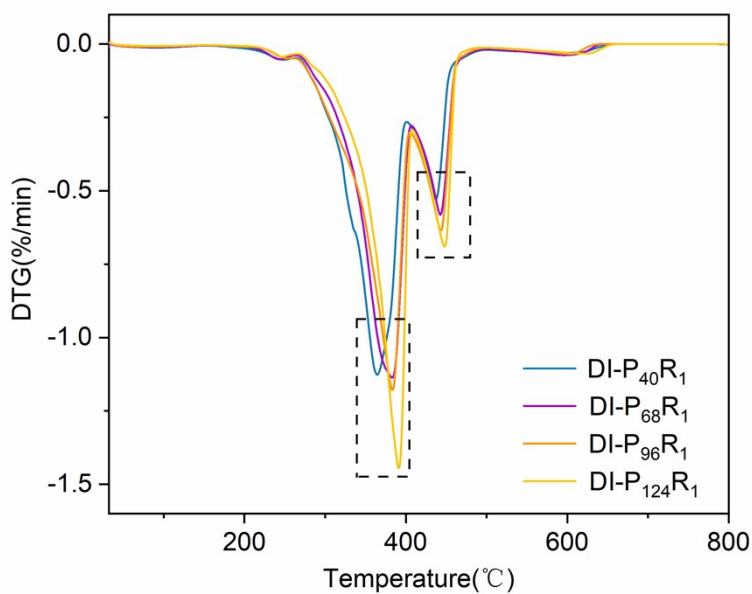
Fig. S9 Derivative thermogravimetry of four DI-PR gels from 25–100 °C (N_2 atmosphere). Initial decomposition temperatures in the first weight loss phase at 227.4, 223.5, 254.8 and 245.2 °C,

respectively, are indicative of oxime-carbamate dynamic covalent bond dissociation. The starting temperatures of the second weight loss stage were 332.1, 341.9, 348.8 and 359.4 °C, respectively. The starting temperatures of the third weight loss stage were 430.2, 430.5, 429.6 and 432.6 °C, respectively, and the thermal decomposition temperature increased as the proportion of P was increased.
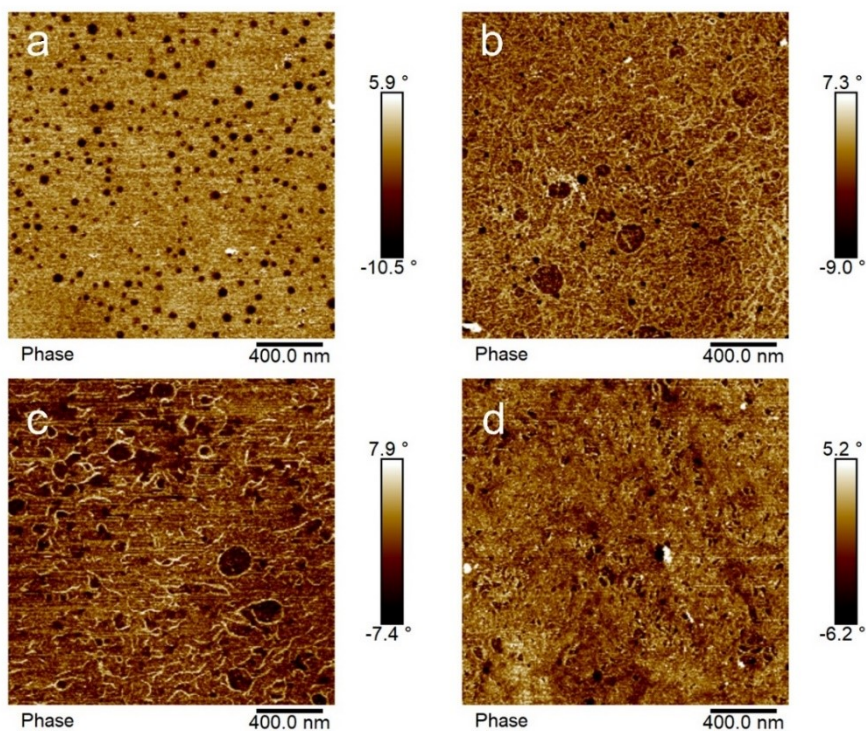

Fig. S10 Two-dimensional atomic force microscopy phase diagrams of DI-PR gels. (a) Two-dimensional phase diagram of DI-$P_{40}R_1$. The overall color of the image is brighter for polymers incorporating only soft-chain PCL530, but does not show a discernible hard-phase microdomain structure. Instead, there is a phase inversion, which means that the soft segments are dispersed in a matrix composed of hard segments, and the aggregation of soft chains does not act as a physical cross-linking point for the hard chains; (b) two-dimensional phase diagram of DI-$P_{68}R_1$ showing blurred hard-segmented microcrystalline phases as the proportion of P is increased; (c) two-dimensional phase diagram of DI-$P_{96}R_1$. At this higher proportion of P, the bands between light and dark are sharper, indicating a higher degree of microphase separation and more stable hard-segmented microregions; (d) two-dimensional phase diagram of DI-$P_{124}R_1$. The proportion of P is too high, resulting in dissolution of the hard phase and absence of the microphase separation structure.
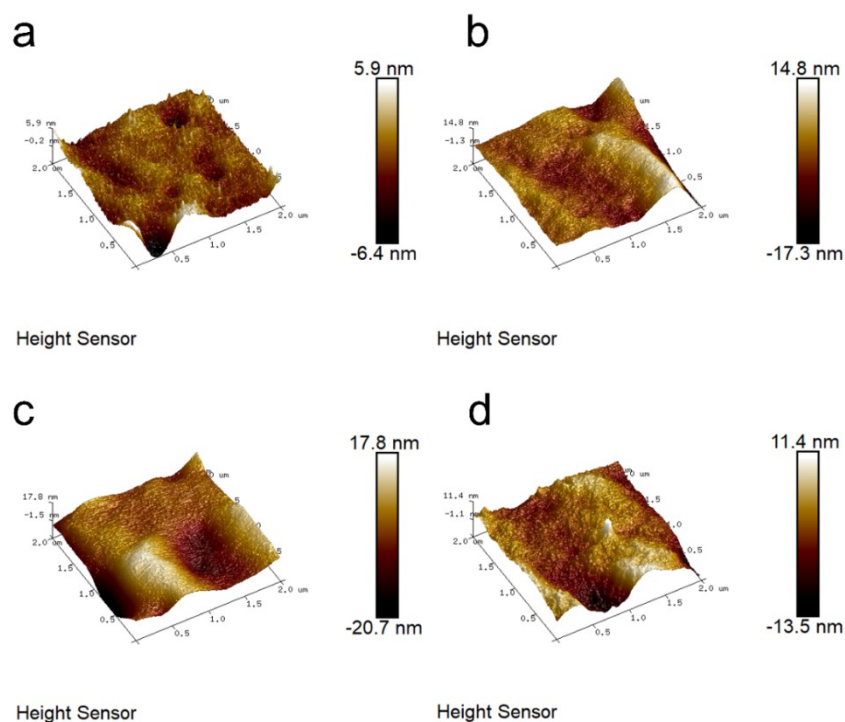
Fig. S11 Three-dimensional atomic force microscopy phase diagrams of DI-PR gels. (a) Three-dimensional phase diagram of DI-$P_{40}R_1$; (b) three-dimensional phase diagram of DI-$P_{68}R_1$. The surface has large height variations in addition to protrusions. Surface roughness increased from 12.3 nm for DI-$P_{40}R_1$ to 32.1 nm for DI-$P_{68}R_1$, which affects migration of the chain segments. The higher proportion of P increases the roughness of the ionic liquid gel and increases the degree of microphase separation in the system; (c) three-dimensional phase diagram of DI-$P_{96}R_1$. Surface roughness is further increased, with height variations between −20.7 and 17.8 nm, and there is more pronounced height variation; (d) three-dimensional phase diagram of DI-$P_{124}R_1$. Since the proportion of P is too high, the surface roughness is decreased.
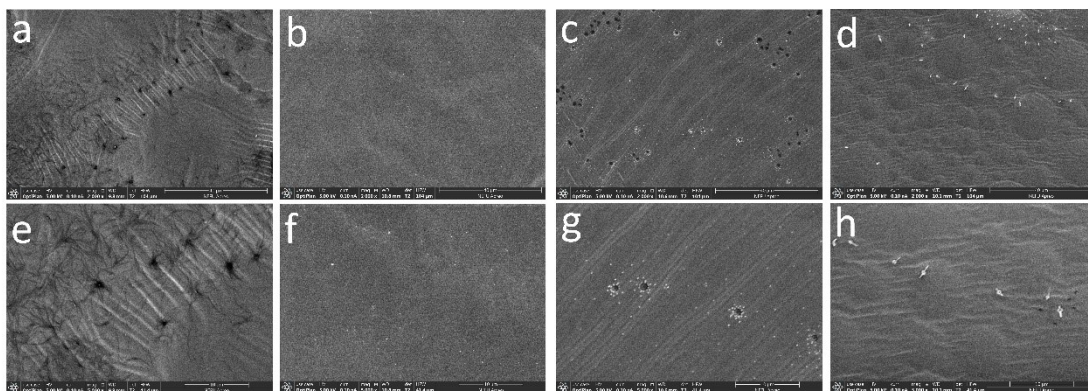
Fig. S12 SEM images of DI-PR gels. (a, e) SEM images of DI-P$_{40}$R$_1$. The microphase separation structure is uniformly distributed and the interface is obvious. The degree of hydrogen bonding and the proportions of hard and soft segments will affect microphase separation. The thermodynamic incompatibility of hard and soft segments leads to microphase separation of the ionic liquid gel. When the polymer contains only PCL530, the soft phase shows dense and fiber-crosslinked morphology, but the boundary of the microphase structure is fuzzy and the light and dark partitions are not obvious; (b, f) SEM images of DI-P$_{68}$R$_1$. As the proportion of P is increased, the microphase separation structure becomes more pronounced, forming a more obvious "sea-island" structure; (c, g) SEM images of DI-P$_{96}$R$_1$. When n(P):n(R) = 96:1, the interface between soft and hard phases is more obvious and the microphase separation structure is gradually homogenized. The agglomerated particles are uniformly dispersed in the continuous phase with an island structure. The best mechanical properties are observed when physical and chemical cross-linking reach a certain equilibrium. This is because the microphase separation structure helps the ionic liquid gel to withstand and transfer stresses, optimizing the strength and toughness of the material; (d, h) SEM images of DI-P$_{124}$R$_1$. As the proportion of P is further increased, the difference between hard and soft phases becomes more significant. The hard phase aggregates and the block size becomes larger, while the soft phase dissolves the hard phase and the microphase separation structure is no longer homogeneous and obvious.
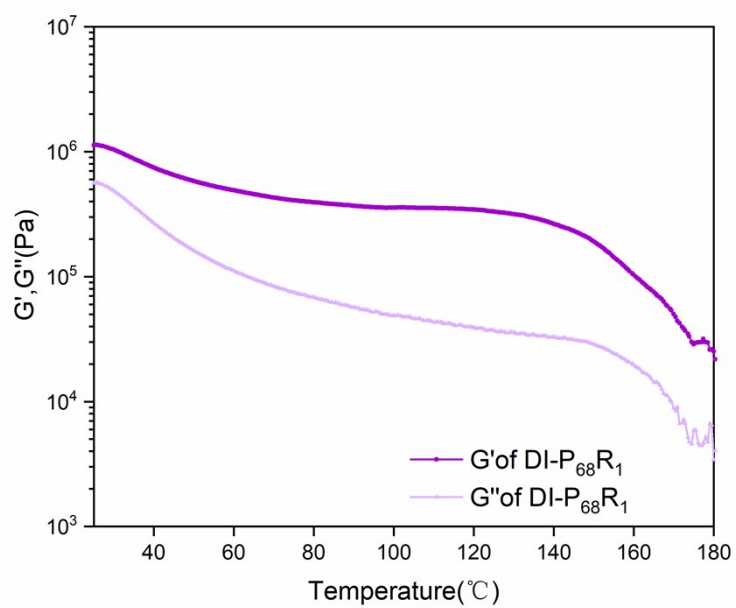
Fig. S13 The energy storage modulus (G') and loss modulus (G") of DI-$P_{68}R_1$. From 140–170 °C, both G' and G'' decrease by about an order of magnitude.
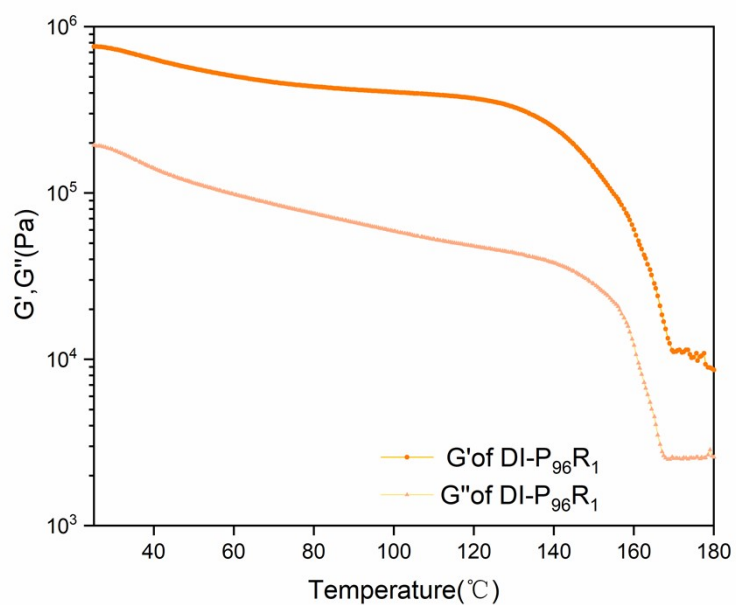

Fig. S14 The energy storage modulus (G') and loss modulus (G") of DI-$P_{96}R_1$. From 140–170 °C, both G' and G'' decrease by about an order of magnitude.
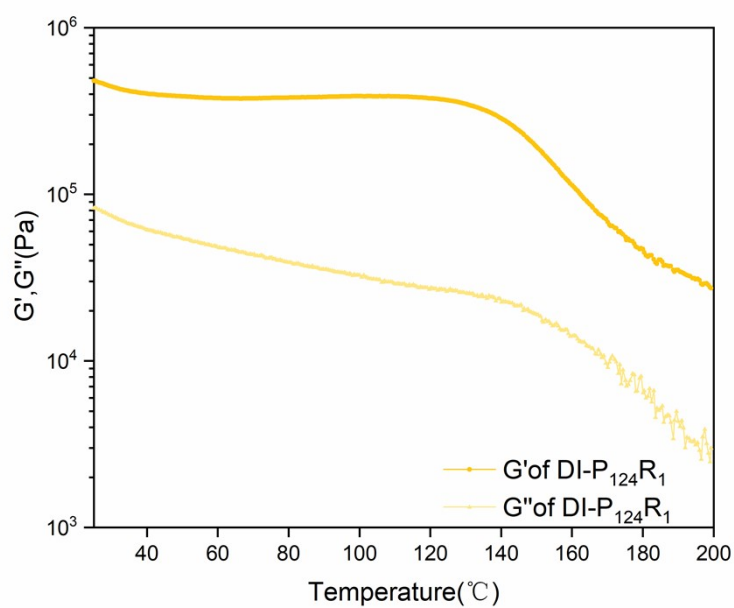
Fig. S15 The energy storage modulus (G') and loss modulus (G") of DI-P$_{124}$R$_1$. From 140–170 °C, both G' and G'' decrease by about an order of magnitude.
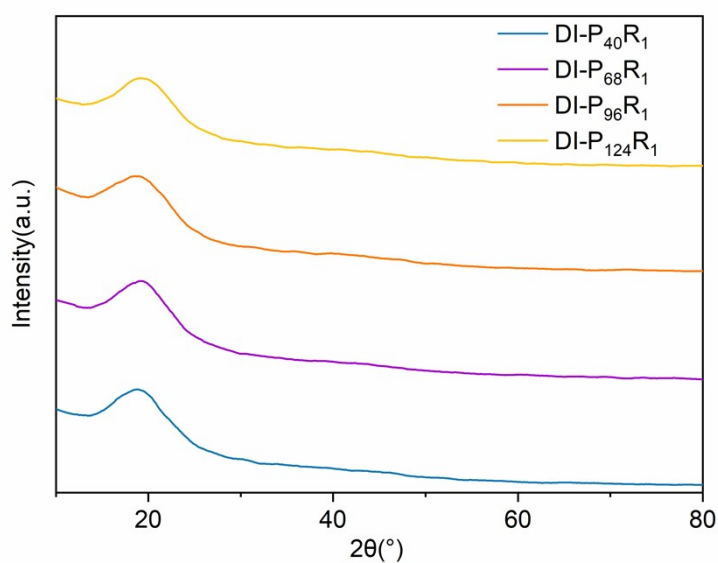

Fig. S16 XRD spectra of four DI-PR gels. The XRD spectra showed broad peaks at $2\theta = 20°$, which are indicative of amorphous structures.
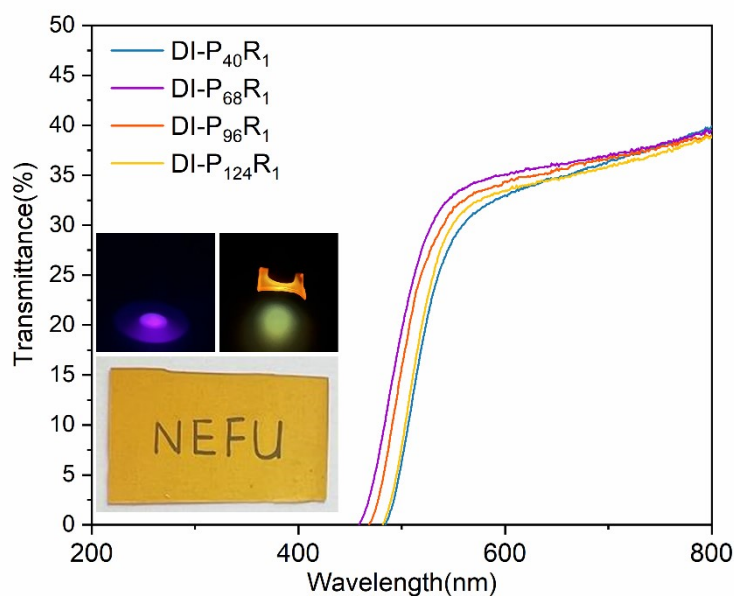
Fig. S17 UV-Vis spectra of four DI-PR gels (inset shows photographs of blank UV irradiation under dark conditions, UV transmission through an DI-$P_{96}R_1$, and DI-$P_{96}R_1$ under visible light). There is zero transmittance at wavelengths of 200–450 nm, which is due to the large number of conjugated double bonds in rutin, and absorption of ultraviolet light in the long, middle and short wavelength bands is greater than 90%. A conjugated structure is also present in [EMIM][NTf_2], which contributes to the absorption of ultraviolet light. Consequently, transmittance of ultraviolet light by the ionic liquid gel is 0%, demonstrating that the ionic liquid gel has potential as a UV protective material. Interestingly, the transmittance of the high-energy visible (HEV) band of the blue-violet spectrum (400–450 nm) was also 0%, which may be due to the yellow color of rutin. HEV is known to be the main cause of light-induced eye diseases and chronic retinal damage, and blue light in this part of the spectrum is potentially hazardous to the human eye. It is therefore apparent that the ionic gel has potential for use in UV-short wave blue light shielding materials, such as anti-blue light protective film for electronic products.
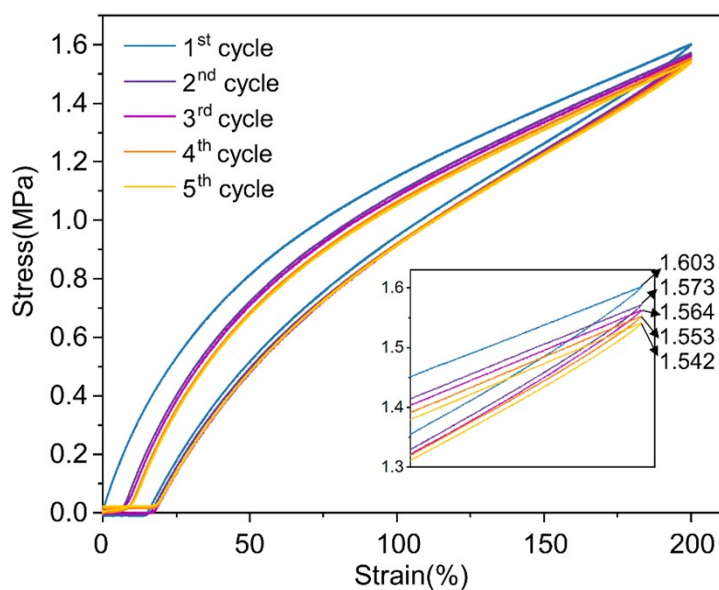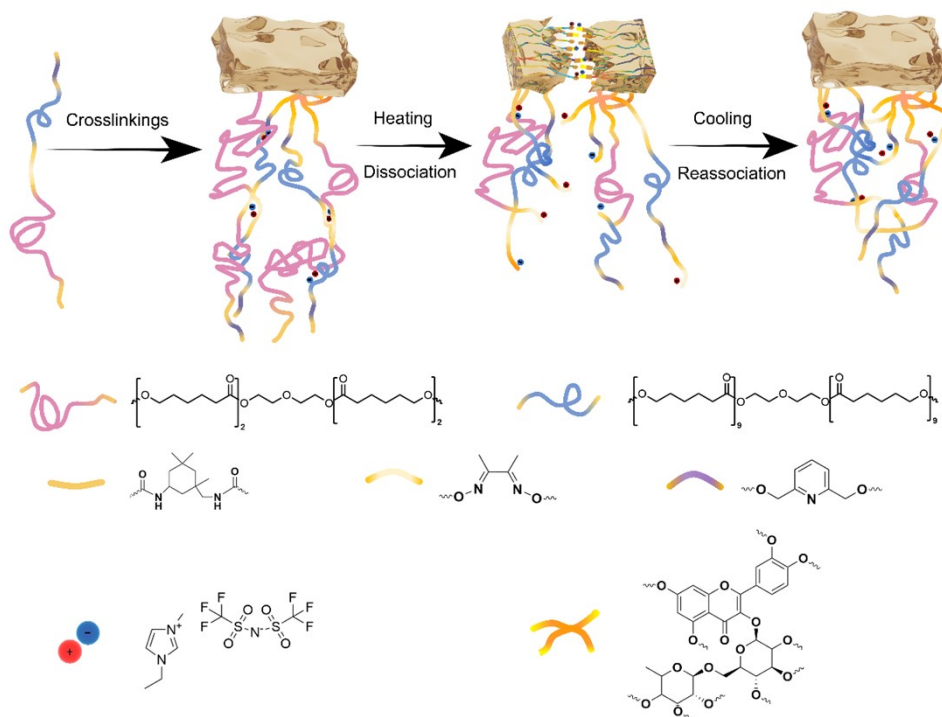
Fig. S18 Cyclic loading and unloading tensile curves of DI-P$_{96}$R$_1$ at 200% fixed strain over 5 cycles (Insert is a magnified view of the strain at 190% to 200%).
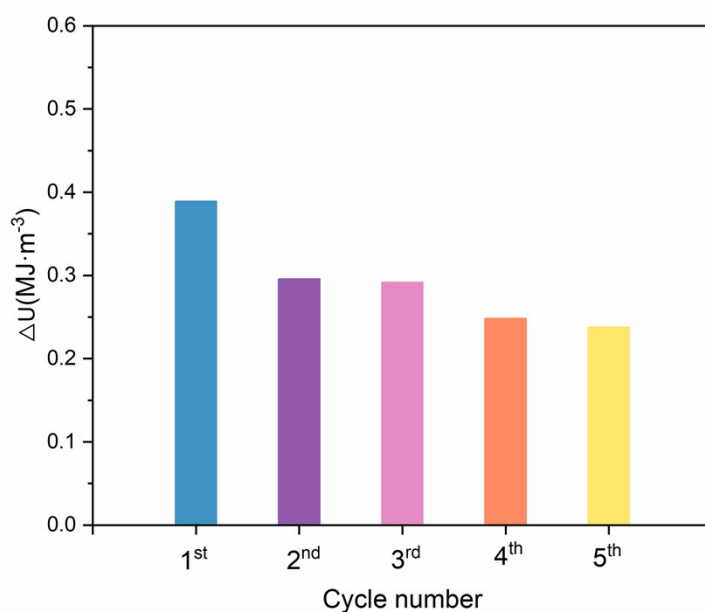
Fig. S19 Dissipated energy for the loading-unloading cycles shown in Fig. S18. The dissipated energy essentially remains at 65% of the initial level from the third cycle onwards.

Fig. S20 Schematic showing self-healing of DI-PR gels. The yellow lines represent the dynamic oxime-carbamate covalent bond. The red and blue balls represent [EMIM][NTf$_2$], which dissociate at high temperatures, thus reducing the degree of cross-linking. When the temperature is lowered, bonds indicated by the yellow lines re-form, the red and blue balls aggregate again, and crosslinking is re-established.
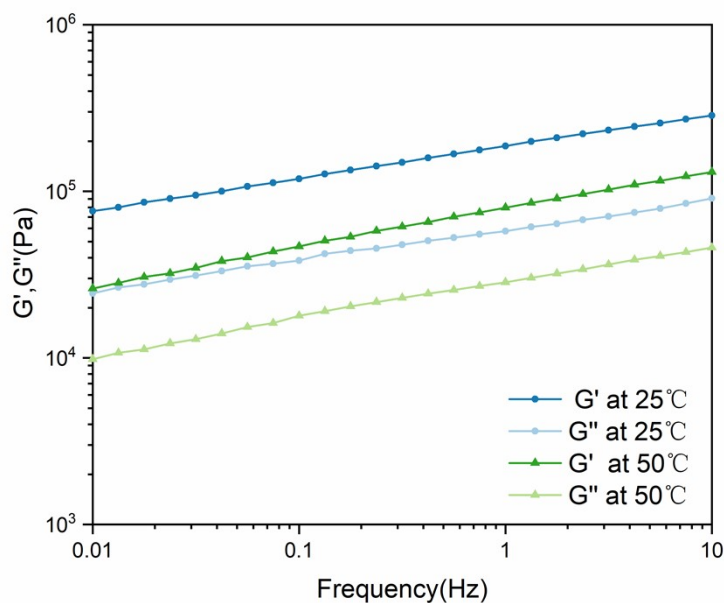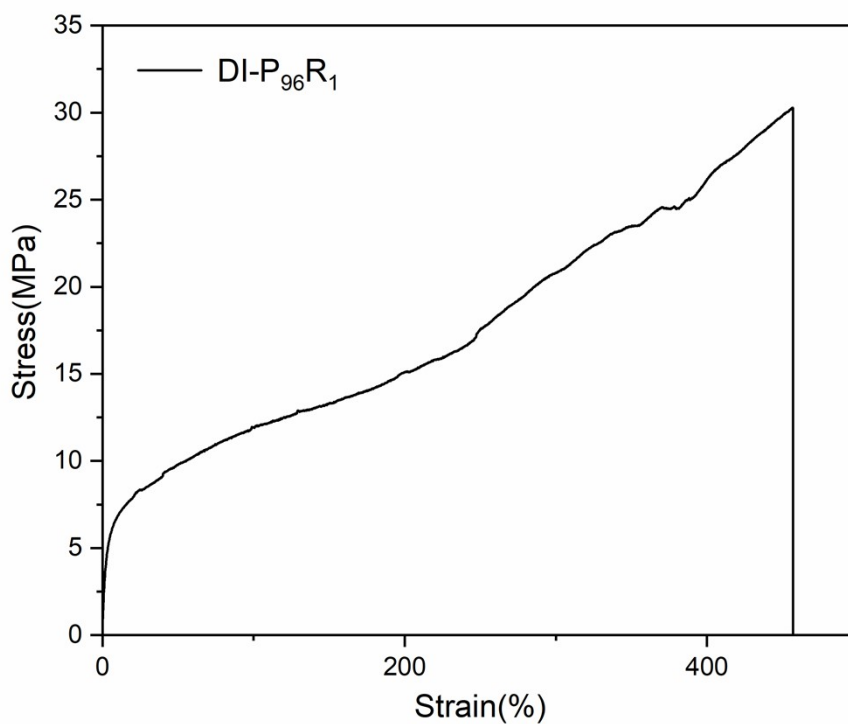

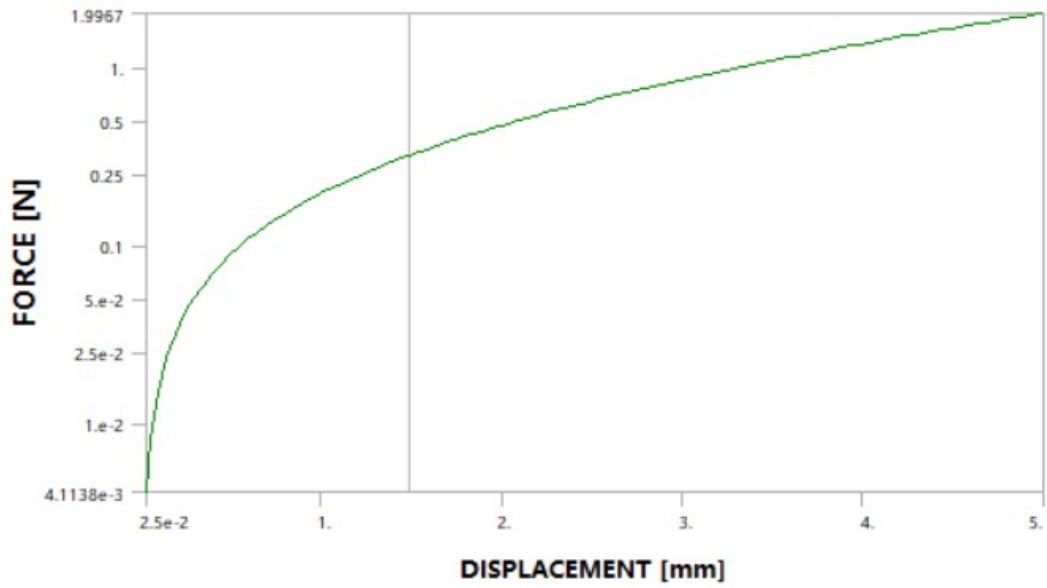**Fig. S21** G' and G'' of DI-P$_{40}$R$_1$ at 25 and 50 °C. G' is higher than G'', indicating that DI-P$_{40}$R$_1$
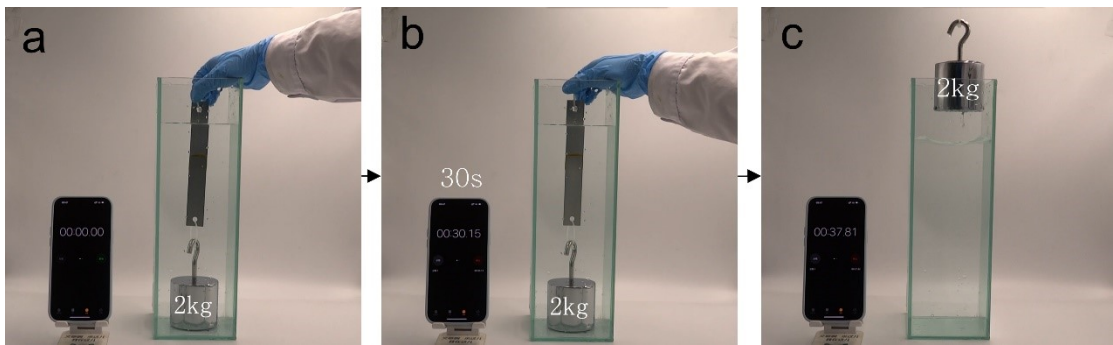
exhibits elastic behavior at lower temperatures.
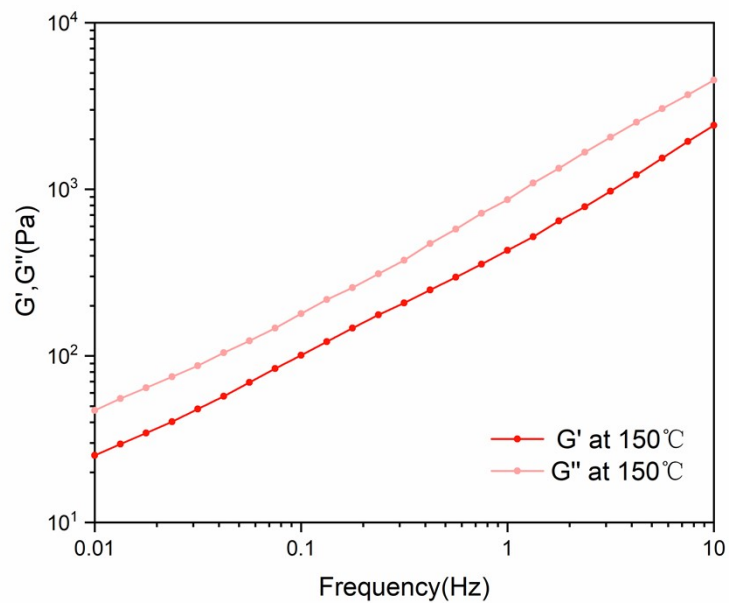
Fig. S22 G' and G'' of DI-P$_{40}$R$_1$ at 150 °C. G" is higher than G', indicating that DI-P$_{40}$R$_1$ exhibits fluidic behavior at 150 °C.


**Fig. S23** Stress-strain curve of DI-P$_{96}$R$_1$ at −50 °C.

Fig. S24 Peeling force curve with displacement.

Fig. S25 Photographs of a gel-bonded high-strength steel plate lifting a 2 kg weight from water after immersion in water for 30 s. (a) Digital photograph of a gel-bonded high-strength steel plate freshly immersed in water; (b) digital photograph of a gel-bonded high-strength steel plate immersed in water for 30 s; (c) digital photograph of a gel-bonded high-strength steel plate being lifted from the water into air after immersion in water for 30 s.
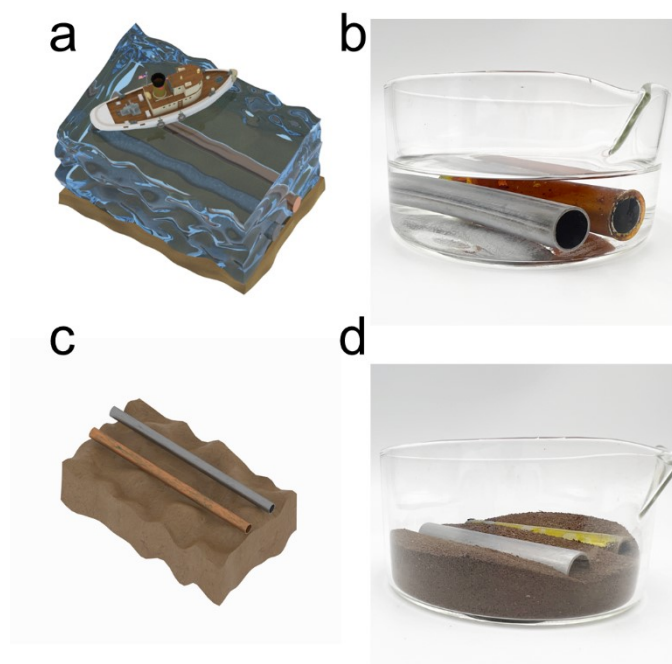
Fig. S26 Illustrations of submarine and underground pipelines. (a) Schematic diagram of submarine pipeline; (b) photograph of simulated submarine pipeline; (c) schematic diagram of underground pipeline; (d) photograph of simulated underground pipeline.
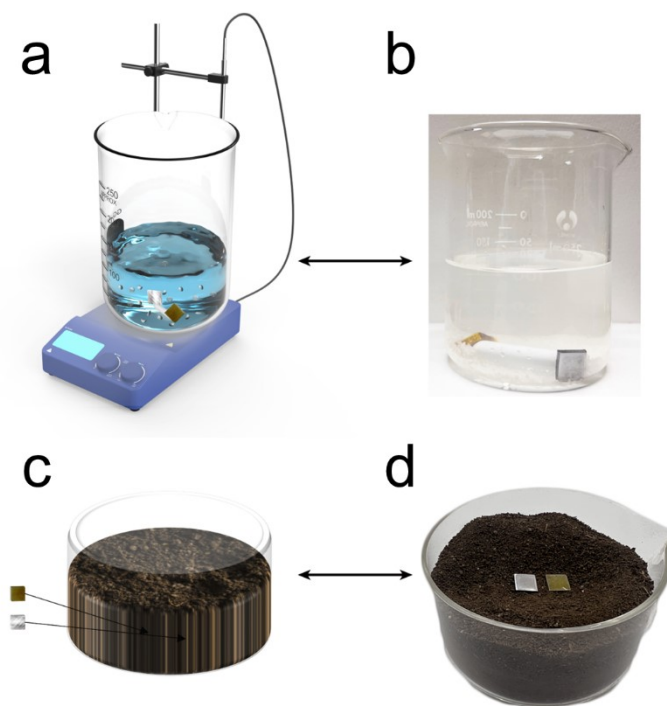

Fig. S27 Immersion experiments in artificial seawater and soil. (a) Schematic diagram of immersion experiments in simulated seawater; (b) photograph of immersion experiment in simulated seawater; (c) schematic diagram of burial experiments in simulated soil; (d) photograph

of burial experiment in simulated soil.
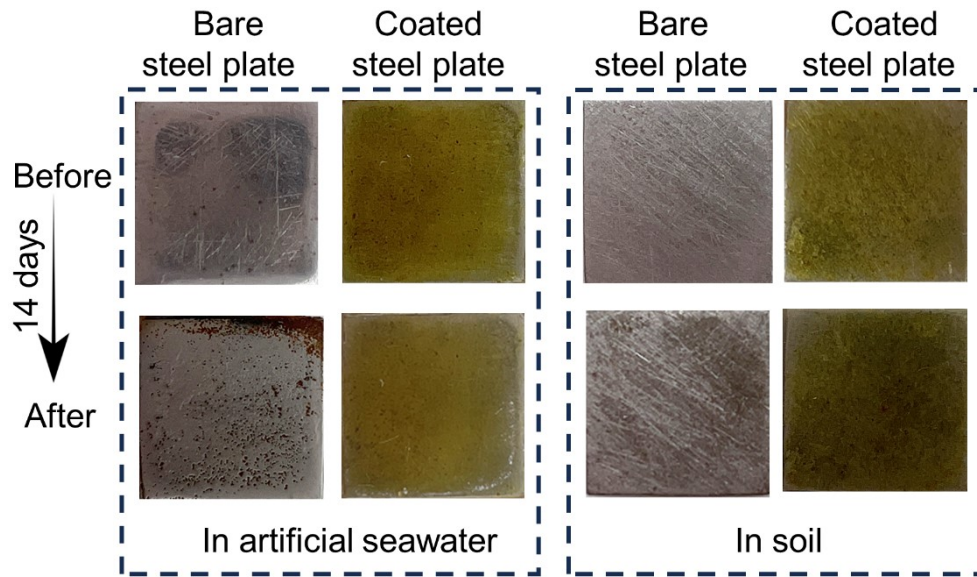
Fig. S28 Surface changes of bare and coated steel plates before and after 14 days in simulated seawater and soil. After immersion in artificial seawater for 14 days, a bare steel plate was severely corroded and the surfaces were rusty and pitted. Under the same conditions, a DI-PR-coated steel plate remained flat, with no obvious surface corrosion. Similar results were seen when the steel sheets were buried in soil; after 14 days, the bare sheet showed traces of corrosion, whereas the DI-PR-coated steel plate remained flat and showed no traces of corrosion.
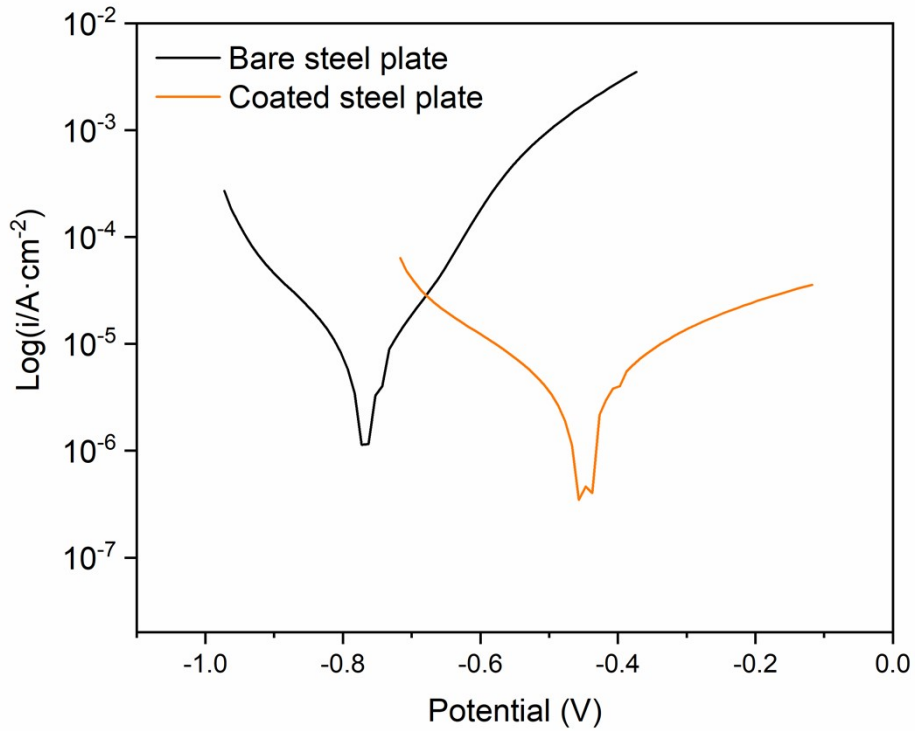
Fig. S29 Tafel curves of bare and coated steel plates after immersion in 3.5 wt.% NaCl solution. The corrosion potential (Ecorr) of the DI-PR-coated steel plate (−0.48 V) is positively shifted compared with that of the bare steel plate (−0.76 V). The corrosion current density (Icorr) of the bare steel plate was 5.87×10^{-6} A·cm^{-2}, compared with 3.50×10^{-6} A·cm^{-2} for the DI-PR-coated steel plate.
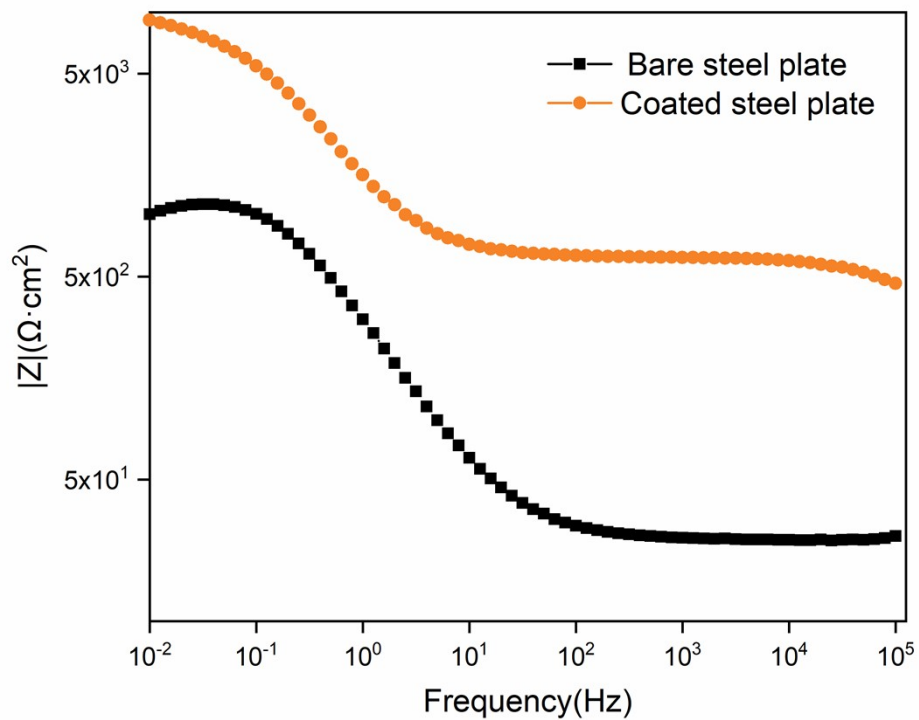
Fig. S30 Bode plots (|Z| vs. frequency) for bare and coated steel plates after immersion in 3.5 wt.% NaCl. The |Z| value of the DI-PR-coated steel plate was an order of magnitude higher than that of the bare steel plate at a frequency of 0.01 Hz. Higher |Z| values at lower frequency indicate greater corrosion resistance.
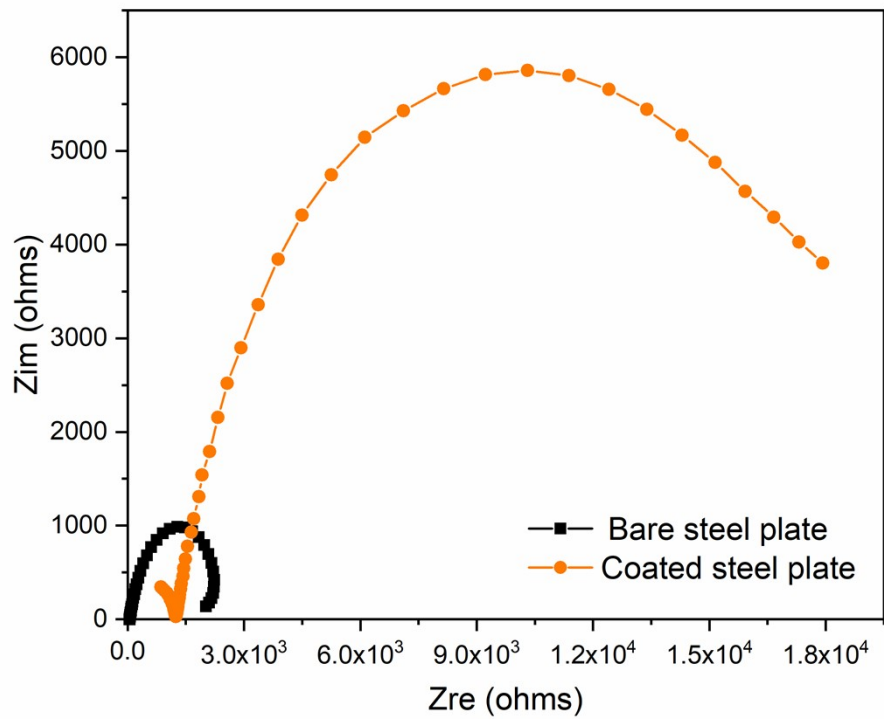
Fig. S31 Nyquist plots of uncoated and coated steel plate samples after 2 h immersion in 3.5 wt.% NaCl. The semicircular impedance arc of the DI-PR-coated steel plate is significantly larger than that of the bare steel plate, suggesting that the DI-PR coating significantly enhances resistance to polarization and thus protects against corrosion.

3 Supplementary Movies

Movie S1. Rapid recovery of ionic liquid gel after stretching

Movie S2. Rapid self-healing of DI-PR after cutting

Movie S3. Simulation of 90° peeling experiment

Movie S4 Gel-bonded high-strength steel plates moving from water to air

4 Supplementary Table

Table S1. Quantities used in syntheses of ionic liquid gels

Sample	PCL530 (g)	PCL2000 (g)	IPDI (mL)
DI-P$_{40}$R$_1$	2.120	0	1.585
DI-P$_{68}$R$_1$	1.696	1.6	1.585
DI-P$_{96}$R$_1$	1.272	3.2	1.585
DI-P$_{124}$R$_1$	0.848	4.8	1.585

Table S2. Interfacial toughness with different cell sizes

Unit size /mm	Interfacial toughness (J m^{-2})
1	1865.7
0.9	1792.2
0.8	1542.2
0.7	1423.6
0.6	1601.9
0.5	1507.8
0.4	1536.5
0.3	1424.3
0.2	1537.1
0.1	1477.1

Table S3. Simulation model parameters

model parameter	numerical value
μ_1(kPa)	25.769
α_1	3.5034
r	0.313678
m(kPa)	4.064724
β	0.544188
$S_{interface}$(kPa)	200
δ_{max}(mm)	3

Table S4. Electrochemical parameters derived from polarization curves, illustrating that the coating has a corrosion protection efficiency of 40.4%

Sample	I$_{corr}$(A·cm^{-2})	E$_{corr}$(V)	η（%）
Bare steel plate	5.87×10^{-6}	-0.76	
Coated steel plate	3.5×10^{-6}	-0.48	40.4%

Reference

1   H. Yuk , T. Zhang , S. T. Lin, G. A. Parada ,X. H. Zhao, Tough bonding of hydrogels to diverse

non-porous surfaces, *Nature mater.*, 2016, **15**(2) ,190-196.